RESEARCH ARTICLE

LASER & PHOTONICS REVIEWS

www.lpr-journal.org

Tunable Vector Polarization Transformation Enabled by Meta-Cavity

Chen Chen, Chunyi Niu, Wange Song, Shining Zhu, Tao Li, and Din Ping Tsai**

Polarization transformation plays a key role in applications of photonics and quantum optics. Traditional bulky optical components are inadequate for miniaturized systems, while metasurfaces offer a revolutionary solution, but still face challenges with vector polarization tunability. Here, a tunable vector polarization transformation mechanism is introduced, utilizing a bifacial metasurfaces enabled meta-cavity. By adjusting the cavity length and phase modulations to achieve complex interferences of two spin light, diverse vector polarization transformations are demonstrated on higher-order and hybrid-order Poincaré spheres. The results outline a powerful paradigm to realize vector polarization transformations in a tunable way and can open new possibilities for applications in optical communications, encryption, and beyond.

1. Introduction

Polarization refers to the trajectory of the electric field vector, and its on-demand manipulation is a momentous basis in various domains, from imaging and optical displays to sensing and quantum optics.[1–3] Traditional methods of polarization control mainly rely on bulky and natural optical components, which often fall short of the demands of miniaturization and complex functionalities. In recent years, metasurfaces[4,5] have emerged as a groundbreaking solution for polarization manipulation, owing to their ultra-thin, lightweight, and highly flexible properties. Composed of subwavelength-scale nano-structure arrays, metasurfaces can manipulate the amplitude, phase, polarization state, and angular momentum of light by precisely designing the geometry and material properties of these nano-structures.[6–10]

To date, various achievements in polarization manipulation using metasurfaces have been reported,[11,12] including polarization transformation,[13,14] polarization beam splitting,[15,16] polarization detection,[17,18] polarization-assisted holography,[19–22] imaging,[23,24] and encryption.[25,26] Among these, polarization transformation, which aims to convert a simple polarization state into a specific state or complex distribution, is itself quite fascinating and essential for enabling other advanced applications.

Existing research has demonstrated significant progress of static polarization transformation in optical working band, achieving functionalities such as linear/circular polarizers,[13,14] half-wave/quarter-wave plates,[27–29] longitudinal polarization transformation,[30,31] full/solid Poincaré sphere polarizers,[32,33] vector polarization generation,[34–38] and so forth. In partnership with phase change materials,[39,40] device orientation,[41] voltage-controlled indium tin oxide,[42] and liquid crystal[43] contribute to achieving uniform polarization transformation tunability. However, challenges still remain in realizing vector polarization transformation tunability to date, mainly due to necessity for simultaneous complex phase modulation and tunable capabilities. The realization of tunable vector polarization transformation not only fulfills the requirements for real-time adjustments and multifunctional integration but also paves the way for more sophisticated and intelligent optical systems.

In this study, we propose a tunable vector polarization transformation mechanism based on a meta-cavity constructed from bifacial metasurface and their chiral-symmetry components. The bifacial metasurface features spin-dependent transmission and reflection.[44] By adjusting the cavity length, a global phase for one of the spin lights can be accumulated, thereby modulating the interference between the two spin lights. By implementing different phase modulations to the bifacial metasurface, we demonstrate vector polarization transformations on both the higher-order and hybrid-order Poincaré spheres. We envision this work

C. Chen, C. Niu, W. Song, S. Zhu, T. Li
National Laboratory of Solid State Microstructures
Key Laboratory of Intelligent Optical Sensing and Manipulations
Jiangsu Key Laboratory of Artificial Functional Materials
College of Engineering and Applied Sciences
Nanjing University
Nanjing 210093, China
E-mail: taoli@nju.edu.cn

C. Chen, D. P. Tsai
Department of Electrical Engineering
City University of Hong Kong
Kowloon, Hong Kong SAR 999077, China
E-mail: dptsai@cityu.edu.hk

D. P. Tsai
State Key Laboratory of Terahertz and Millimeter Waves
City University of Hong Kong
Kowloon, Hong Kong SAR 999077, China

D. P. Tsai
Centre for Biosystems, Neuroscience, and Nanotechnology
City University of Hong Kong
Kowloon, Hong Kong SAR 999077, China

The ORCID identification number(s) for the author(s) of this article can be found under https://doi.org/10.1002/lpor.202500434

DOI: 10.1002/lpor.202500434

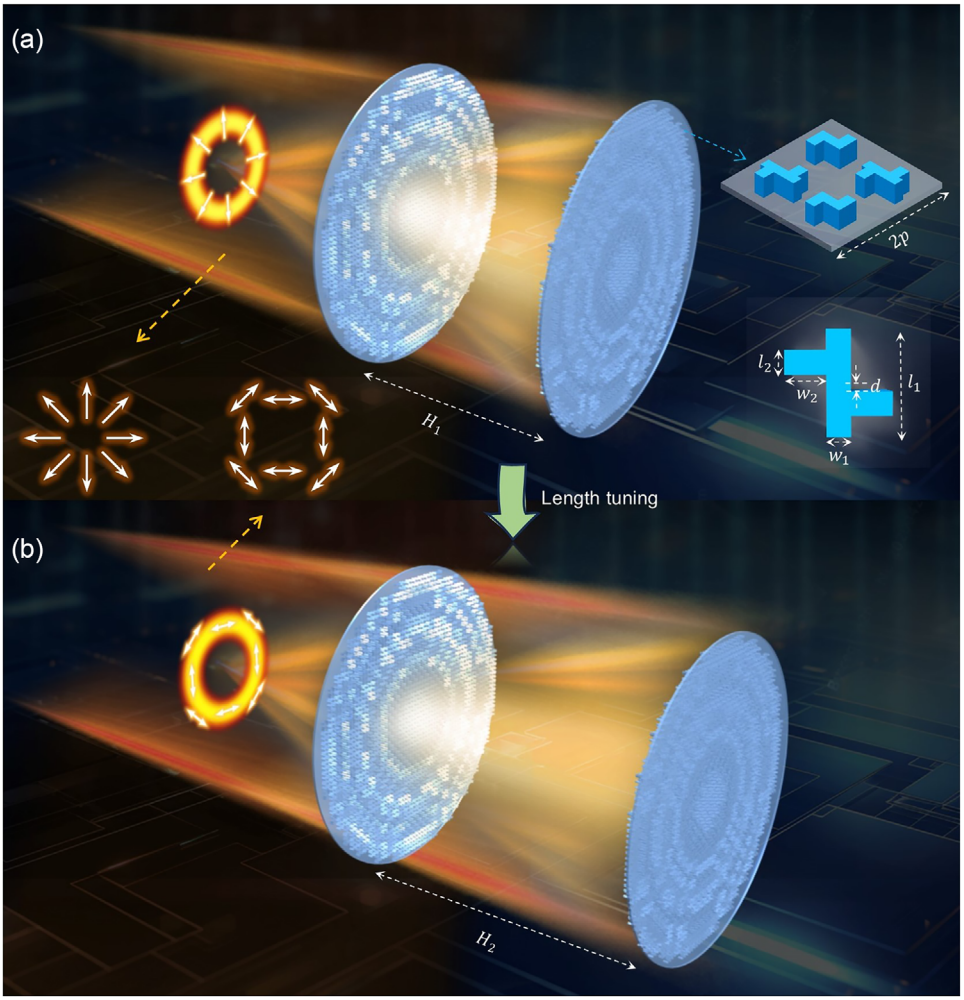

Figure 1. Schematic of the tunable polarization transformation enabled by the meta-cavity. a) and b) illustrate different scenarios of polarization transformation achieved by adjusting the cavity length. The right panel of (a) depicts the supercell construction along with the structural parameters of the individual chiral meta-atom.

to inspire new directions in the development of polarization-tunable devices.

2. Results

2.1. Working Principle: Meta-Cavity with Bifacial Metasurfaces

Figure 1 illustrates the operating principle of the tunable vector polarization manipulation based on the meta-cavity. Light is incident on the first layer (the left metasurface in Figure 1a) of the meta-cavity. Half of this light (e.g. the left circularly polarized light (LCP) component) is directly modulated to reflect, while the other half (the orthogonal part, e.g. the right circularly polarized light (RCP) component) enters the meta-cavity and reflects off the second modulation layer (the right metasurface in Figure 1a). This reflected light then transmits through the first layer and interferes with the initially reflected light. The interference of these two orthogonal components can construct arbitrary polarization state, including uniform and vector polarizations.

As shown in Figure 1b, tuning the cavity length alters the optical path of the light component entering the cavity (e.g. RCP), leading to a global phase change, and results in a flexible manipulation of the interfered polarization state. By implementing suitable amplitude contrasts and spatially local phase modulations to the two orthogonal light components, different trajectories of polarization transformation on the higher-order and hybrid-order Poincaré spheres[45,46] can be achieved through cavity length tuning.

To achieve the exquisite transmission-reflection modulation, we employed our previous design strategy based on bifacial metasurfaces.[44] This bifacial metasurface consists of a pair of staggered twin meta-atoms with a total period of $2p$ (see the right panel in Figure 1a). Planar chiral meta-atoms,[47] which break the mirror symmetry and n-fold($n > 2$) rotational symmetry are selected for versatile spin light manipulation. The variable structural parameters for chiral meta-atoms are illustrated in the lower right corner of Figure 1a, including the sizes of central rod (w_1, l_1), the two arm rods (w_2, l_2), and the distance between them (d). Each individual meta-atom can independently modulate the phase $\varphi^{\pm}$

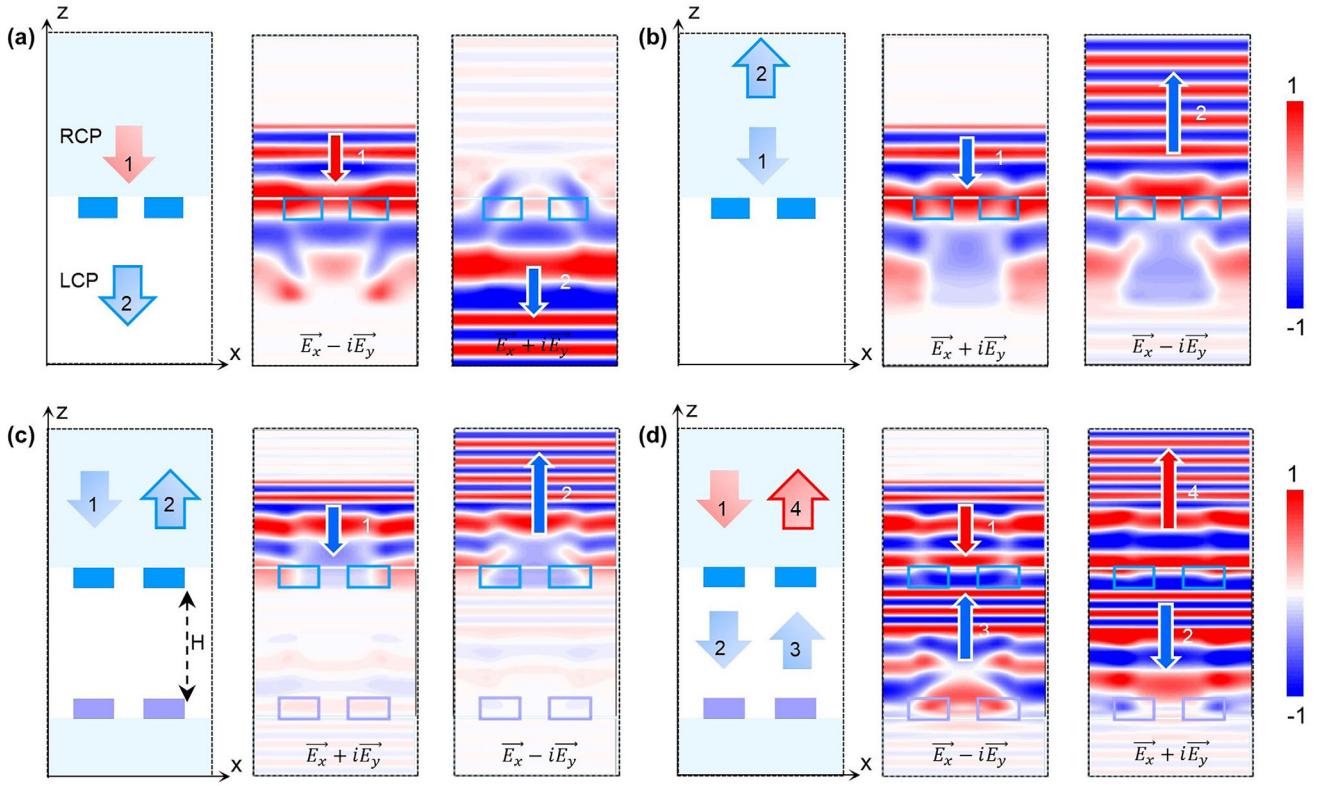

Figure 2. Electric field simulation results. a) The bifacial supercell (marine blue) under right circular polarization (RCP) incidence from the substrate (baby blue), and b) under left circular polarization (LCP) incidence. The left panel displays the schematic diagram, while the middle and right panels show the decomposed electric fields. c) The meta-cavity composed of the bifacial supercell (marine blue) and its chiral-symmetry component (lilac) under LCP incidence from the top layer, and d) under RCP incidence. H is the cavity length.

for different spin states (with + and − indicating RCP/LCP light) while maintaining nearly identical high transmittance. When the supercell period $2p$ is subwavelength, collective interference results in a total scattered electric field that can be expressed as

$$E^{\pm} = \sqrt{2 + 2\cos\left(\varphi_1{}^{\pm} - \varphi_2{}^{\pm}\right)}\, e^{i\frac{\varphi_1{}^{\pm} + \varphi_2{}^{\pm}}{2}} \quad (1)$$

This indicates that by controlling the phase difference and accumulations of the staggered meta-atoms, we can simultaneously achieve the required spin-dependent transmission (constructive interference) and reflection (destructive interference) modulation (details see Note S1, Supporting Information).

For proof-of-concept, the working wavelength is set at 1550 nm. The supercell period $2p$ is chosen to be 1200 nm to satisfy subwavelength requirement. The refractive indices of the meta-atom material and substrate are 3.47 and 1.74, respectively. The height of the meta-atom is established at 1800 nm to ensure sufficient phase change. The electrical field responses of the meta-atoms and the corresponding supercells are simulated using finite difference time domain methods.

From the constructed meta-atom library, we select a bifacial supercell with parameters $w_1 = 120/120$ nm, $l_1 = 480/270$ nm, $w_2 = 120/140$ nm, and $d = 10/15$ nm for illustration. **Figure** 2a,b displays the spin-dependent transmission and reflection. When RCP light is incident from the substrate (Figure 2a), it transmits to LCP light with a planar wavefront. The numbers indicate the sequence of occurrence, and the arrow colors represent different spin states (red for RCP and blue for LCP). The left panel illustrates the working process, while the middle and right panels show the decomposed electrical field components (Ex-iEy for RCP and Ex+iEy for LCP when propagating from top to bottom, vice versa). When the incidence switches to LCP (Figure 2b), it reflects directly. Notably, if the supercell period is not subwavelength, although reflection can occur due to destructive interference, maintaining a planar wavefront becomes challenging.

By combing the bifacial metasurface with its chiral-symmetry component (see schematics in Figure S6, Supporting Information), we can further construct a meta-cavity with spin-dependent response. Figure 2c shows the situation with LCP incidence, similar to Figure 2b. In the case of RCP incidence, as depicted in Figure 2d, the light first transmits to LCP (marked as 2) upon passing through the first layer. It then reflects off the second layer while maintaining its LCP state (marked as 3). Finally, it transmits through the first layer again and turns back into RCP (marked as 4). This meta-cavity design is different from the traditional cavity definition,[48,49] and also features fewer interactions with interfaces compared to our previous setup that utilized a mirror,[44] making it advantageous for controlling the interference between the total RCP and LCP components.

2.2. Tunable Vector Polarization Transformation on Higher-Order Poincaré Sphere

When the incidence is linearly polarized, the initial decomposed RCP and LCP components exhibit the same amplitude contrast. After interacting with the meta-cavity without pre-designed local phase distribution, the interfered polarization can be described as

$$|P\rangle = A_L |L\rangle + A_R e^{i\varphi(H)} |R\rangle \quad (2)$$

in which A_L and A_R are the modulated amplitudes of the LCP and RCP components reflected from the meta-cavity, φ is the modulated global phase related to the cavity length H (shown in Figure 2c), and the initial phases are omitted for simplicity. By applying supercells with $A_L = A_R \approx 1$(e.g. the one shown in Figure 2), the optical rotation effect[50] can be realized with total efficiency up to 99%. If $A_L \neq A_R$, the uniform polarization transformation would move from the equator of Poincaré sphere[51] to the other trajectories on the surface. Details can be found in Note S2 (Supporting Information).

With pre-designed local phase distribution to the spin lights, spatially varying polarization state, dubbed as vector polarization can be further achieved. For demonstration, we next implemented vortex phase modulations in the bifacial metasurfaces to achieve vector polarization transformation. The synthetic polarization state can be expressed as:

$$|P\rangle = |L, l\rangle + e^{i\varphi(H)} |R, m\rangle \quad (3)$$

where l and m denote the topological charges of the LCP and RCP components, respectively. The vortex phase associated with l and m can be expressed as $\varphi_{\mathrm{LCP}} = l \arctan(y/x)$, and $\varphi_{\mathrm{RCP}} = m \arctan(y/x)$. If $l = m$, the polarization state resides on the equator of higher-order Poincaré Sphere (HOPS),[45] and varying the cavity length causes movement along the equator. If $l \neq m$, the hybrid-order Poincaré Sphere (HyOPS)[46] can describe the synthetic states, with the dynamic transformation similarly achievable by controlling the $\varphi(H)$.

Figure 3 illustrates the results of vector polarization transformation on the HOPS with $l = 1$. The bifacial supercells are rotated to meet the vortex phase requirements based on PB phase.[52,53] This rotation induces a spatial phase change related to the rotation angle without affecting the bifacial effect. The second layer of the meta-cavity maintains chiral symmetry with the first layer, featuring the same spin light response when incident from opposite directions. The metasurface has a diameter of 36 μm and employs a perfectly matched layer boundary condition. The cavity length is set as 2, 3, and 4 μm for efficient simulation. Under LCP incidence, the reflectance is ≈93%. Figure 3a presents the simulation results of the meta-cavity, with the top row showing the reflected phase distribution and the bottom row displaying the real part of the electric field distribution. These results remain nearly unchanged with varying H, consistent with our bifacial metasurface design. In the case of RCP incidence, there are two additional transmission paths, resulting in a slightly lower reflectance of ≈82%. Due to the intrinsic symmetry of the PB phase, the final vortex phase retains the same topological charge (+1). As shown in Figure 3b, the vortex phase profile along with the real part electrical field distribution rotates with the varying cavity length, indicating the manipulation of $\varphi(H)$.

To perform the vector polarization transformation, we changed the incidence back to x polarization, as illustrated in Figure 3c. Eight evenly spaced point detectors (Figure S7, Supporting Information) are placed on the reflection surface to extract field data for polarization calculations. The total efficiency is ≈89%. The upper row displays the calculated vector polarization from the simulations, with red representing right-handedness (S3 > 0), blue indicating left-handedness (S3 < 0), and black denoting pure linearly polarized features with abs(S3) <0.01. The polarization ellipse distribution precisely describes the ellipticity and azimuth angle at each simulated point position, with particular emphasis on the azimuth angle that defines the engineered linear polarization orientation. To establish theoretical consistency, we constructed a 3 × 3 electric field matrix according to the vortex phase information of the HOPS, from which the Stokes parameters were also systematically calculated to draw the polarization ellipse distribution. Different phase delays were intentionally introduced between the RCP and LCP field components to align theoretical predictions with simulated azimuth angle profiles. The bottom row presents the approximate theoretical calculations of the vector polarization distribution, which positioned along the equator of the HOPS for comparison, other typical distributions are shown in Figure S8 (Supporting Information). Thanks to the nearly ideal modulation efficiencies of the meta-cavity cells, the light oscillations between the two metasurfaces are very weak, and have minimal effect on the final interfered vector polarization. The agreement between simulation and theoretical calculation demonstrates the feasibility of dynamically controlling vector polarization on the HOPS. While only three distinct vector polarization distributions are explicitly shown, the continuous variation of the cavity length fundamentally enables seamless adjustability throughout the vector polarization transformation process.

2.3. Tunable Vector Polarization Transformation on Hybrid-Order Poincaré Sphere

Furthermore, by combining the PB phase with different bifacial supercells, we can achieve independent phase modulation for various spin light incidences. We set $\varphi_{\mathrm{LCP}} = 0$ in reflection mode and $\varphi_{\mathrm{RCP}} = \arctan(y/x)$ in transmission mode for the first bifacial metasurface (details of the design can be found in Note S3 and Table S1, Supporting Information). The second layer of the meta-cavity is also the corresponding chiral-symmetry components. **Figure 4a** presents the simulation results under LCP incidence with a reflectance of ≈87%. Due to the uniform modulation, both the phase and the real part of the electrical field exhibit minimal spatial variation, as shown in the upper row and lower row, respectively. These distributions also remain consistent with varying H. Under RCP incidence, the light transmits through the first metasurface twice, yielding a final reflectance of ≈65%. This also results in acquiring the vortex phase twice, leading to a topological charge of 2. As depicted in Figure 4b, the phase transitions from $-\pi$ to π and back again. The increase of cavity length also leads to the global rotation of the electrical field distribution, corresponding to $\varphi(H)$ in Equation (3). When the

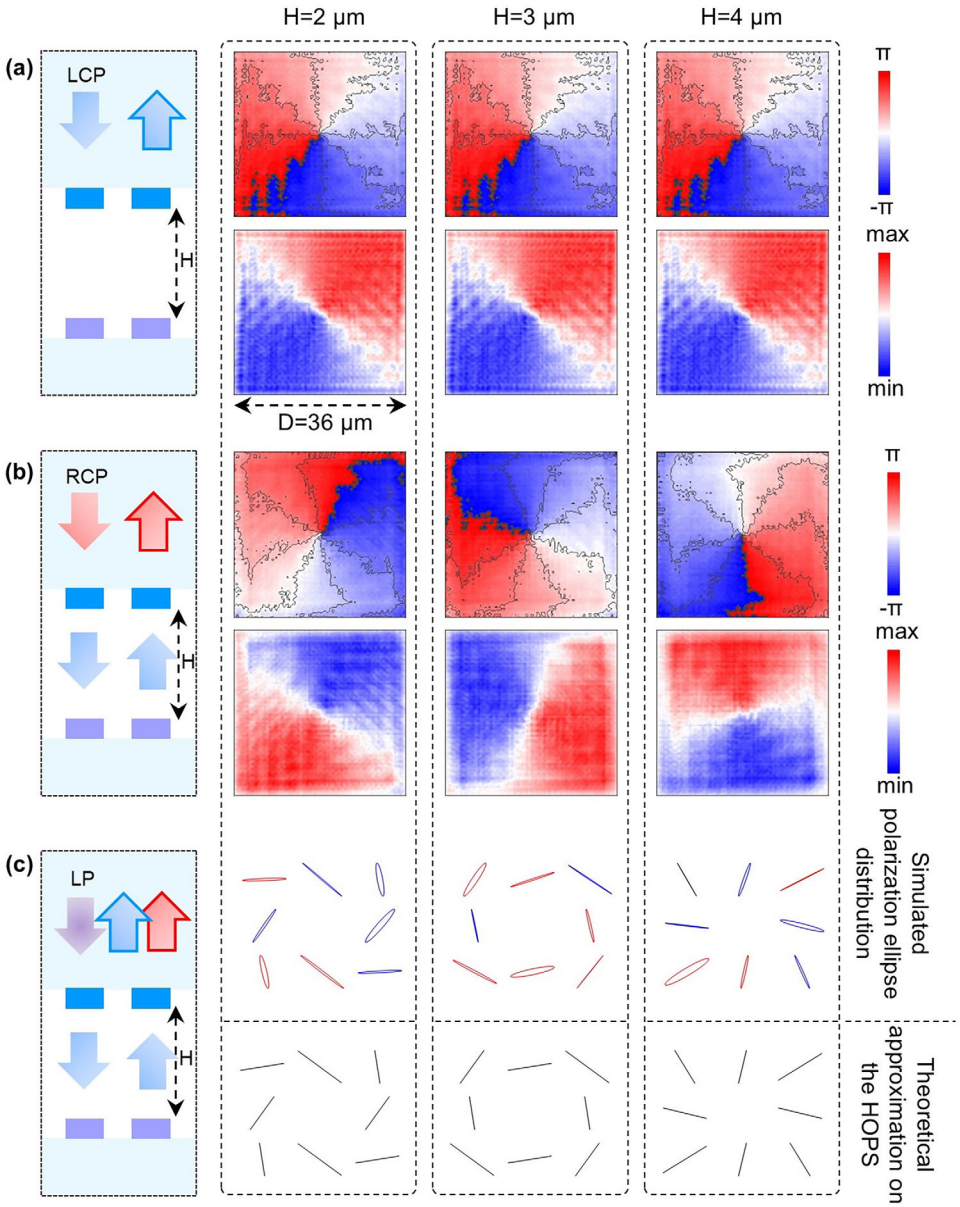

Figure 3. Vector polarization transformation on the higher-order Poincaré Sphere (HOPS). a) Reflected electric field results of the meta-cavity under LCP incidence. The left panel shows the schematic diagram, while the right panel displays field profiles with varying cavity lengths; the upper row represents the phase, and the lower row shows the real part of the field. b) Reflected electric field results under RCP incidence. c) Vector polarization transformation results under *x*-polarization incidence, with the upper row showing the spatial polarization ellipse distribution calculated from the simulated results, and the lower row presenting the approximate theoretical distributions on the HOPS.

incidence switches to x polarization, the synthetic polarization aligns with the vector state on the HyOPS with $l = 0$ and $m = 2$ (see Equation (3)). The total reflectance is ≈82%, fall between the reflectances observed under LCP and RCP incidences. The upper row of Figure 4c displays the calculated vector polarization state based on simulations, which shows different distributions with varying values of H. The distinctness of the elliptical polarizations can be attributed to the decreased modulation efficiency arising from the breakdown of perfect periodic boundary conditions, in which the light oscillation effect would also emerge. The theoretical approximations were similarly calculated as discussed in Section 2.2. Nevertheless, the overall morphologies of the simulation results closely resemble the theoretical results presented in the lower row of Figure 4c, indicating the effectiveness of the vector state transformation on the HyOPS.

3. Conclusion

In conclusion, we proposed a tunable vector polarization transformation method based on meta-cavity. The meta-cavity is constructed by a bifacial metasurface and its chiral-symmetry components, and features pre-designed times of light interaction.

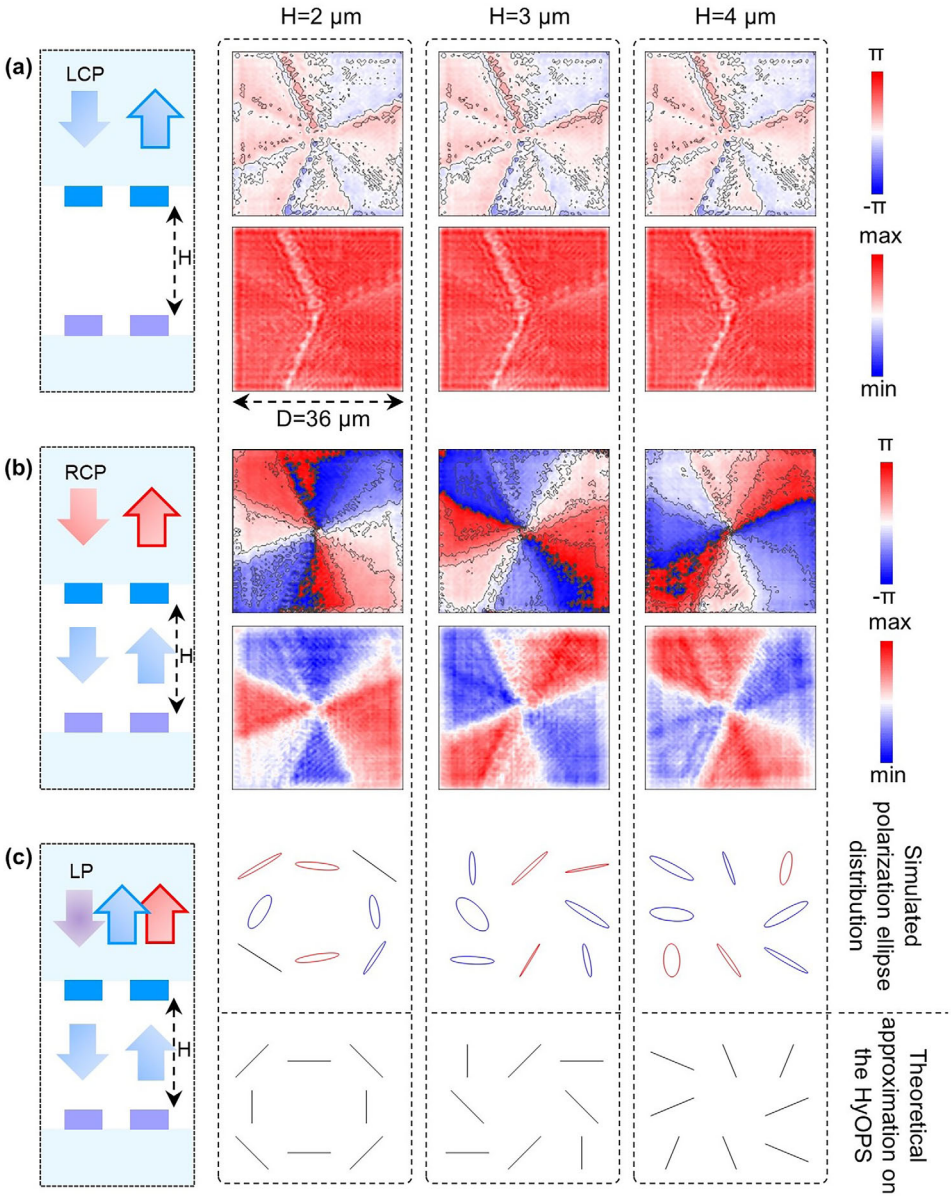

Figure 4. Vector polarization transformation on the hybrid-order Poincaré Sphere (HyOPS). a) Reflected electric field results of the meta-cavity under LCP incidence. The left panel shows the schematic diagram, while the right panel displays field profiles with varying cavity lengths; the upper row represents the phase, and the lower row shows the real part of the field. b) Reflected electric field results under RCP incidence. c) Vector polarization transformation results under *x*-polarization incidence, with the upper row showing the spatial polarization ellipse distribution calculated from the simulated results, and the lower row presenting the approximate theoretical distributions on the HyOPS.

Tuning the cavity length would result in a global phase change of one spin light and affect the final interfered polarization state from the meta-cavity. By implementing different phase modulations to the bifacial metasurfaces, we demonstrated vector polarization transformations on both the higher-order and hybrid-order Poincaré Spheres, and the tunability is facilitated by cavity length adjustments. More complex vector polarization transformations are also possible with particularly designed bifacial metasurfaces. To further enhance the current efficiencies, some optimization algorithms like gradient descent algorithm can be introduced to optimize the current optional bifacial supercells combination to minimize the coupling and cross-talk between each other and maximize the total modulation efficiency. As demonstrated in Figures S9–S12 (Supporting Information), the method also exhibits robust polarization controllability under practical parameter deviations including cavity thickness fluctuations, incident angle misalignment, and anisotropy axis misalignment or displacement, prosming the real-world applications. In future experiments, the cavity length tuning can be achieved through direct mechanical movement, or by using voltage-controlled MEMS[54] and liquid crystal[55] technologies. The MEMS system would similarly adjust the

physical cavity length, whereas the liquid crystal would modify the effective cavity length by changing the effective refractive index. This work could advance the miniaturization of vector polarization transformation devices and inspire further innovative applications based on bifacial metasurfaces.

4. Experimental Section

Numerical Simulation: Numerical simulations were performed using finite difference time domain (FDTD) methods. The optical constants of the materials were obtained from the software for Al_2O_3 and monocrystalline silicon. Periodic boundary conditions were applied in both the *x* and *y* directions, while perfectly matched layer boundary conditions were implemented in the *z* direction for simulations of bifacial unit cells and meta-cavities without additional phase modulations. For simulations involving meta-cavities with additional phase modulations, perfectly matched layer boundary conditions were applied in all directions. The excitation source was configured as either a left-circularly polarized, right-circularly polarized, or *x*-polarized plane wave.

Supporting Information

Supporting Information is available from the Wiley Online Library or from the author.

Acknowledgements

This work was supported by the National Key R&D Program of China (2024YFA1012600, 2022YFA1404301), National Natural Science Foundation of China (Nos. 62325504, 62305149, 92250304, 62288101, 12204233), University Grants Committee / Research Grants Council of the Hong Kong Special Administrative Region, China (Project No. AoE/P-502/20, CRF Project: C1015-21E; C5031-22G, GRF Project: CityU11300224; CityU11305223, and City University of Hong Kong (Projects Nos. 9380131).

Conflict of Interest

The authors declare no conflict of interest.

Data Availability Statement

The data that support the findings of this study are available in the supplementary material of this article.

Keywords

bifacial metasurface, higher-order Poincaré sphere, meta-cavity, polarization transformation, vector polarization

Received: February 26, 2025
Revised: April 28, 2025
Published online:

[1] N. S. Holliman, N. A. Dodgson, G. E. Favalora, L. Pockett, *IEEE Trans. Broadcast.* **2011**, *57*, 362.
[2] J. S. Tyo, D. L. Goldstein, D. B. Chenault, J. A. Shaw, *Appl. Opt.* **2006**, *45*, 5453.
[3] M. O. Scully, M. S. Zubairy, *Am. J. Phys.* **1999**, *67*, 648.
[4] N. Yu, P. Genevet, M. A. Kats, F. Aieta, J. P. Tetienne, F. Capasso, Z. Gaburro, *Science* **2011**, *334*, 333.
[5] A. I. Kuznetsov, M. L. Brongersma, J. Yao, M. K. Chen, U. Levy, D. P. Tsai, N. I. Zheludev, A. Faraon, A. Arbabi, N. Yu, D. Chanda, K. B. Crozier, A. V. Kildishev, H. Wang, J. K. W. Yang, J. G. Valentine, P. Genevet, J. A. Fan, O. D. Miller, A. Majumdar, J. E. Fröch, D. Brady, F. Heide, A. Veeraraghavan, N. Engheta, A. Alù, A. Polman, H. A. Atwater, P. Thureja, R. P. Dominguez, et al., *ACS Photonics* **2024**, *11*, 816.
[6] F. Ding, C. Meng, S. I. Bozhevolnyi, *Photonics Insights* **2024**, *3*, R07.
[7] T. Li, C. Chen, X. Xiao, J. Chen, S. Hu, S. Zhu, *Photonics Insights* **2023**, *2*, R01.
[8] T. Gu, H. J. Kim, C. R. Baleine, J. Hu, *Nat. Photonics* **2023**, *17*, 48.
[9] L. Li, L. Gao, Y. Cheng, S. Zhou, J. Wang, H. Yu, C. Gao, S. Fu, *ACS Photonics* **2025**, *12*, 1418.
[10] B. H. Chen, P. C. Wu, V. Su, Y. Lai, C. H. Chu, I. C. Lee, J. Chen, Y. H. Chen, Y. Lan, C. Kuan, D. P. Tsai, *Nano Lett.* **2017**, *17*, 6345.
[11] F. Li, S. Wang, R. Zhong, M. Hu, Y. Jiang, M. Zheng, M. Wang, X. Li, R. Peng, Z. Deng, *Appl. Phys. Rev.* **2024**, *11*, 041332.
[12] Q. Deng, X. Li, M. Hu, F. Li, X. Li, Z. Deng, *npj Nanophotonics* **2024**, *1*, 20.
[13] C. Pelzman, S. Y. Cho, *Appl. Phys. Lett.* **2015**, *106*, 251101.
[14] S. E. Mun, J. Hong, J. G. Yun, B. Lee, *Sci. Rep.* **2019**, *9*, 2543.
[15] M. Khorasaninejad, W. Zhu, K. B. Crozier, *Optica.* **2015**, *2*, 376.
[16] A. Pors, M. G. Nielsen, S. I. Bozhevolnyi, *Optica.* **2015**, *2*, 716.
[17] N. A. Rubin, G. D. Aversa, P. Chevalier, Z. Shi, W. T. Chen, F. Capasso, *Science* **2019**, *365*, aax1839.
[18] C. Chen, X. Xiao, X. Ye, J. Sun, J. Ji, R. Yu, W. Song, S. Zhu, T. Li, *Light: Sci. Appl.* **2023**, *12*, 288.
[19] A. Arbabi, Y. Horie, M. Bagheri, A. Faraon, *Nat. Nanotechnol.* **2015**, *10*, 937.
[20] R. Zhao, B. Sain, Q. Wei, C. Tang, X. Li, T. Weiss, L. Huang, Y. Wang, T. Zentgra, *Light: Sci. Appl.* **2018**, *7*, 95.
[21] Y. Yuan, K. Zhang, B. Ratni, Q. Song, X. Ding, Q. Wu, S. N. Burokur, P. Genevet, *Nat. Commun.* **2020**, *11*, 4186.
[22] B. Xiong, Y. Liu, Y. Xu, L. Deng, C. W. Chen, J. N. Wang, R. Peng, Y. Lai, Y. Liu, M. Wang, *Science* **2023**, *379*, 294.
[23] X. Ye, X. Qian, Y. Chen, R. Yuan, X. Xiao, C. Chen, W. Hu, C. Huang, S. Zhu, T. Li, *Adv. Photonics* **2022**, *4*, 046006.
[24] F. Zhao, R. Lu, X. Chen, C. Jin, S. Chen, Z. Shen, C. Zhang, Y. Yang, *Laser Photonics Rev.* **2021**, *15*, 2100097.
[25] F. Yue, C. Zhang, X. F. Zang, D. Wen, B. D. Gerardot, S. Zhang, X. Chen, *Light: Sci. Appl.* **2018**, *7*, 17129.
[26] Z. L. Deng, M. X. Hu, S. Qiu, X. Wu, A. Overvig, X. Li, A. Alù, *Nat. Commun.* **2024**, *15*, 2380.
[27] F. Ding, Z. Wang, S. He, V. M. Shalaev, A. V. Kildishev, *ACS Nano* **2015**, *9*, 4111.
[28] Y. Li, J. Luo, X. Li, M. Pu, X. Ma, X. Xie, J. Shi, X. Luo, *IEEE Photonics J.* **2020**, *12*, 4600410.
[29] C. Chen, S. Gao, X. Xiao, X. Ye, S. Wu, W. Song, H. Li, S. Zhu, T. Li, *Adv. Photonics Res.* **2021**, *2*, 2000154.
[30] A. H. Dorrah, N. A. Rubin, A. Zaidi, M. Tamagnone, F. Capasso, *Nat. Photonics* **2021**, *15*, 287.
[31] H. Li, S. Duan, C. Zheng, J. Li, H. Xu, C. Song, J. Li, F. Yang, W. Shi, Y. Zhang, Y. Shen, J. Yao, *Adv. Opt. Mater.* **2023**, *11*, 2202461.
[32] S. Wang, Z. L. Deng, Y. Wang, Q. Zhou, X. Wang, Y. Cao, B. O. Guan, S. Xiao, X. Li, *Light: Sci. Appl.* **2021**, *10*, 24.
[33] S. Wang, S. Wen, Z. L. Deng, X. Li, Y. Yang, *Phys. Rev. Lett.* **2023**, *130*, 123801.
[34] F. Yue, D. Wen, J. Xin, B. D. Gerardot, J. Li, X. Chen, *ACS Photonics* **2016**, *3*, 1558.

[35] D. Wen, K. Pan, J. Meng, X. Wu, X. Guo, P. Li, S. Liu, D. Li, B. Wei, X. Xie, D. Yang, J. Zhao, K. B. Crozier, *Laser Photonics Rev.* **2022**, *16*, 2200206.
[36] J. Ji, C. Chen, J. Sun, X. Ye, Z. Wang, J. Li, J. Wang, W. Song, C. Huang, K. Qiu, S. Zhu, T. Li, *PhotoniX* **2024**, *5*, 13.
[37] Y. Bao, J. Ni, C. W. Qiu, *Adv. Mater.* **2020**, *32*, 1905659.
[38] K. Zhang, Y. Wang, Y. Yuan, S. N. Burokur, *Appl. Sci.* **2020**, *10*, 1015.
[39] H. He, H. Yang, Z. Xie, X. Yuan, *Front. Phys.* **2023**, *18*, 12303.
[40] Z. Cai, C. Wu, J. Jiang, Y. Ding, Z. Zheng, F. Ding, *Opt. Express.* **2021**, *29*, 42762.
[41] Z. Yuan, S. H. Huang, Z. Qiao, P. C. Wu, Y. C. Chen, *Optica.* **2023**, *10*, 269.
[42] P. C. Wu, R. Sokhoyan, G. K. Shirmanesh, W. H. Cheng, H. A. Atwater, *Adv. Opt. Mater.* **2021**, *9*, 2100230
[43] P. Yu, J. Li, N. Liu, *Nano Lett.* **2021**, *21*, 6690.
[44] C. Chen, X. Ye, J. Sun, Y. Chen, C. Huang, X. Xiao, W. Song, S. Zhu, T. Li, *Optica* **2022**, *9*, 1314.
[45] G. Milione, H. I. Sztul, D. A. Nolan, R. R. Alfano, *Phys. Rev. Lett.* **2011**, *107*, 053601.
[46] X. Yi, Y. Liu, X. Ling, X. Zhou, Y. Ke, H. Luo, S. Wen, D. Fan, *Phys. Rev. A* **2015**, *91*, 023801.
[47] C. Chen, S. Gao, W. Song, H. Li, S. Zhu, T. Li, *Nano Lett.* **2021**, *21*, 1815.
[48] W. W. Wong, C. Jagadish, H. H. Tan, *IEEE J. of Quantum Electron.* **2022**, *58*, 1.
[49] K. C. Shen, C. T. Ku, C. Hsieh, H. C. Kuo, Y. J. Cheng, D. P. Tsai, *Adv. Mater.* **2018**, *30*, 1706918.
[50] P. L. Polavarapu, *Chirality* **2002**, *14*, 768.
[51] H. Poincaré, *Theorie Mathematique de la Lumiere*, Vol. *2*, Gauthiers-Villars, Paris **1892**.
[52] M. V. Berry, *J. Mod. Opt.* **1987**, *34*, 1401.
[53] L. Huang, X. Chen, H. Mühlenbernd, G. Li, B. Bai, Q. Tan, G. Jin, T. Zentgraf, S. Zhang, *Nano Lett.* **2012**, *12*, 5750.
[54] E. Arbabi, A. Arbabi, S. M. Kamali, Y. Horie, M. F. Dana, A. Faraon, *Nat. Commun.* **2018**, *9*, 812.
[55] Y. V. Izdebskaya, Z. Yang, V. G. Shvedov, D. N. Neshev, I. V. Shadrivov, *Nano Lett.* **2023**, *23*, 9825.